Supporting Information

# Oxygen Evolution Reaction Activity and Underlying Mechanism of Perovskite Electrocatalysts at Different pH

Bae-Jung Kim,[a] Emiliana Fabbri,[a*] Mario Borlaf,[b] Daniel F. Abbott,[a] Ivano E. Castelli,[c] Maarten Nachtegaal,[a] Thomas Graule,[b] and Thomas J. Schmidt[a,d]

[a] Paul Scherrer Institut, Forschungstrasse 111, 5232 Villigen PSI, Switzerland
[b] Laboratory for High Performance Ceramics, Empa, Swiss Federal Laboratories for Science and Technology, 8600 Dübendorf, Switzerland
[c] Department of Energy Conversion and Storage, Anker Engelunds Vej 411, Technical University of Denmark, DK-2800, Kgs. Lyngby, Denmark
[d] Laboratory of Physical Chemistry, ETH Zürich, CH-8093 Zürich, Switzerland
**Corresponding Author**
emiliana.fabbri@psi.ch;

**Table of Contents**



**Table of Figures**

**List of Tables**

**1. Carbonation Effect**

**Table S1.** Carbonation reaction of alkaline electrolyte upon contact with carbon dioxide from the atmosphere.

| | **Cathodic Reaction** | **$E_{rev}$ ($V_{RHE}$)** | **Anodic Reactions** | **$E_{rev}$ ($V_{RHE}$)** |
|---|---|---|---|---|
| | $2H_2O + 2e^- \rightarrow H_2 + 2OH^-$ | 0.000 | $4OH^- \rightarrow O_2 + 2H_2O + 4e^-$ | 1.228 |
| Carbonation | $CO_2 + H_2O + 2e^- \rightarrow CO + 2OH^-$ | -0.100 | $CO_3^{2-} \rightarrow ½\ O_2 + CO_2 + 2e^-$ | 1.520 |
| | $CO_2 + OH^- + \rightarrow HCO_3^-$ | | $2HCO_3^- \rightarrow ½\ O_2 + H_2O + 2CO_2 + 2e^-$ | 1.593 |
| | $HCO_3^- + OH^- \rightarrow H_2O + CO_3^{2-}$ | | | |

Upon carbonation, it is important that the ideal catalyst is capable to facilitate an efficient OER with an overpotential lower than 0.29 V to avoid side reactions that are expected to take place concurrently above 1.52 $V_{RHE}$.

**2. X-ray Diffraction Analysis**

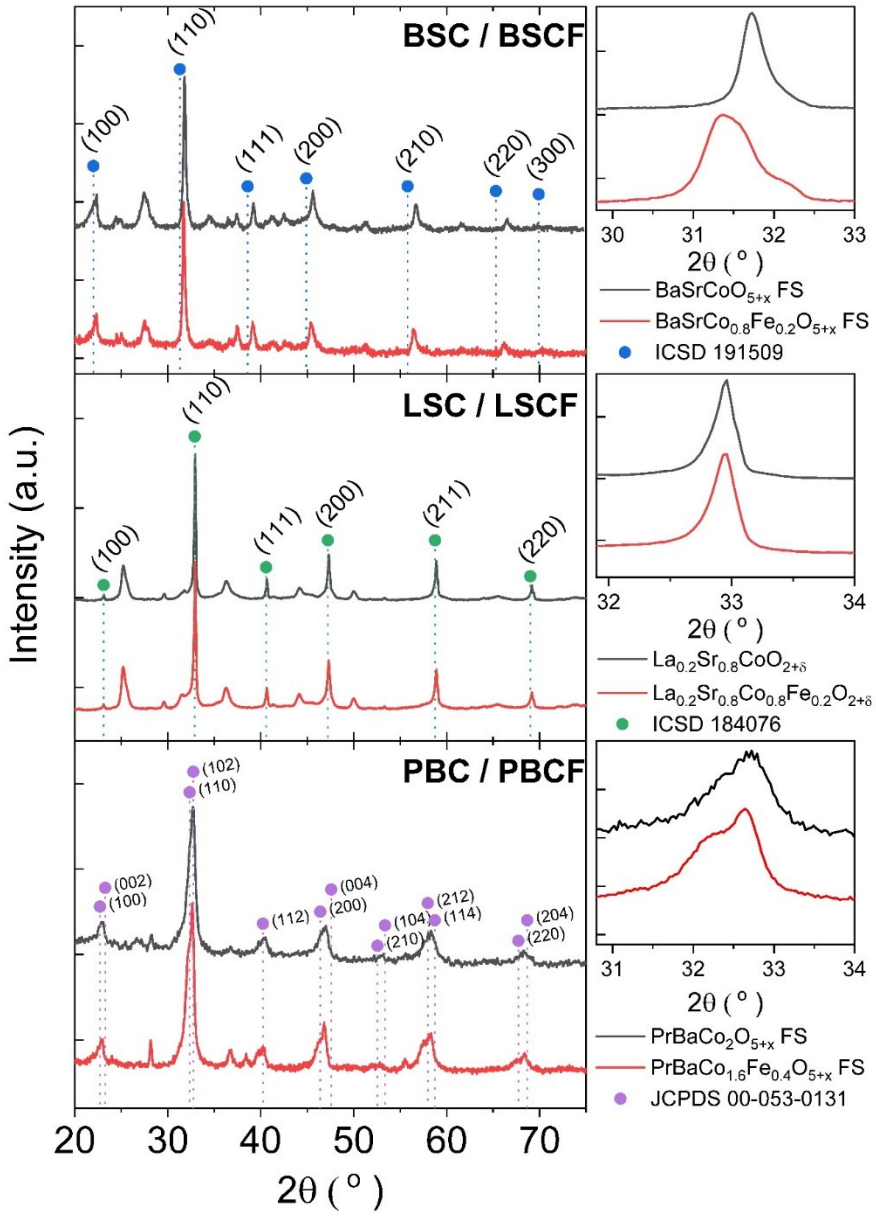


**Figure S1.** Comparison of X-ray diffraction patterns of a) $Ba_{0.5}Sr_{0.5}CoO_{3-\delta}$ and $Ba_{0.5}Sr_{0.5}Co_{0.8}Fe_{0.2}O_{3-\delta}$; b) $La_{0.2}Sr_{0.8}CoO_{3-\delta}$ and $La_{0.2}Sr_{0.8}Co_{0.8}Fe_{0.2}O_{3-\delta}$; and $PrBaCo_2O_{6-\delta}$, $PrBaCo_{1.6}Fe_{0.4}O_{6-\delta}$, and $PrBaCoFeO_{6-\delta}$. Insets in each shows a closer view of (110) peaks.

Figure S1 shows the comparison of X-ray diffraction (XRD) patterns of the prepared perovskites which share the same A-site cations while the B-site either does or does not contain Fe. Figure 1a and b shows these comparisons within the single cubic perovskites: $Ba_{0.5}Sr_{0.5}Co_xFe_{1-x}O_{3-\delta}$ and $La_{0.2}Sr_{0.8}Co_xFe_{1-x}O_{3-\delta}$ (x = 0.8, 1.0), respectively. Regardless to the presence of Fe, all of the prepared single cubic perovskites reveal XRD patterns that are ascribable to the diffraction peaks of their literature cubic perovskites with same composition and similar oxygen vacancies.[1, 2] In addition, Figure S1c shows XRD patterns of $PrBaCo_2O_{6-\delta}$ and $PrBaCo_{1.6}Fe_{0.4}O_{6-\delta}$ those are ascribable to those characteristics of $PrBaCo_2O_{6-\delta}$ (P4/mmm) [JCPDS 00-053-0131]. Nevertheless, commonly for all of the pairs, those perovskites containing Fe in the B-site show peak locations at lower 2-theta values than those without Fe indicating that the former exhibits a relatively larger lattice parameters than the latter. Despite these minor differences, the Fe containing perovskites reveal enhanced performances in both of their activities and stabilities than those without. The functional role of Fe in these perovskites as oxygen evolution reaction catalysts have been exclusively discussed in our previous studies.[3]

**3. Cyclic Voltammetry**

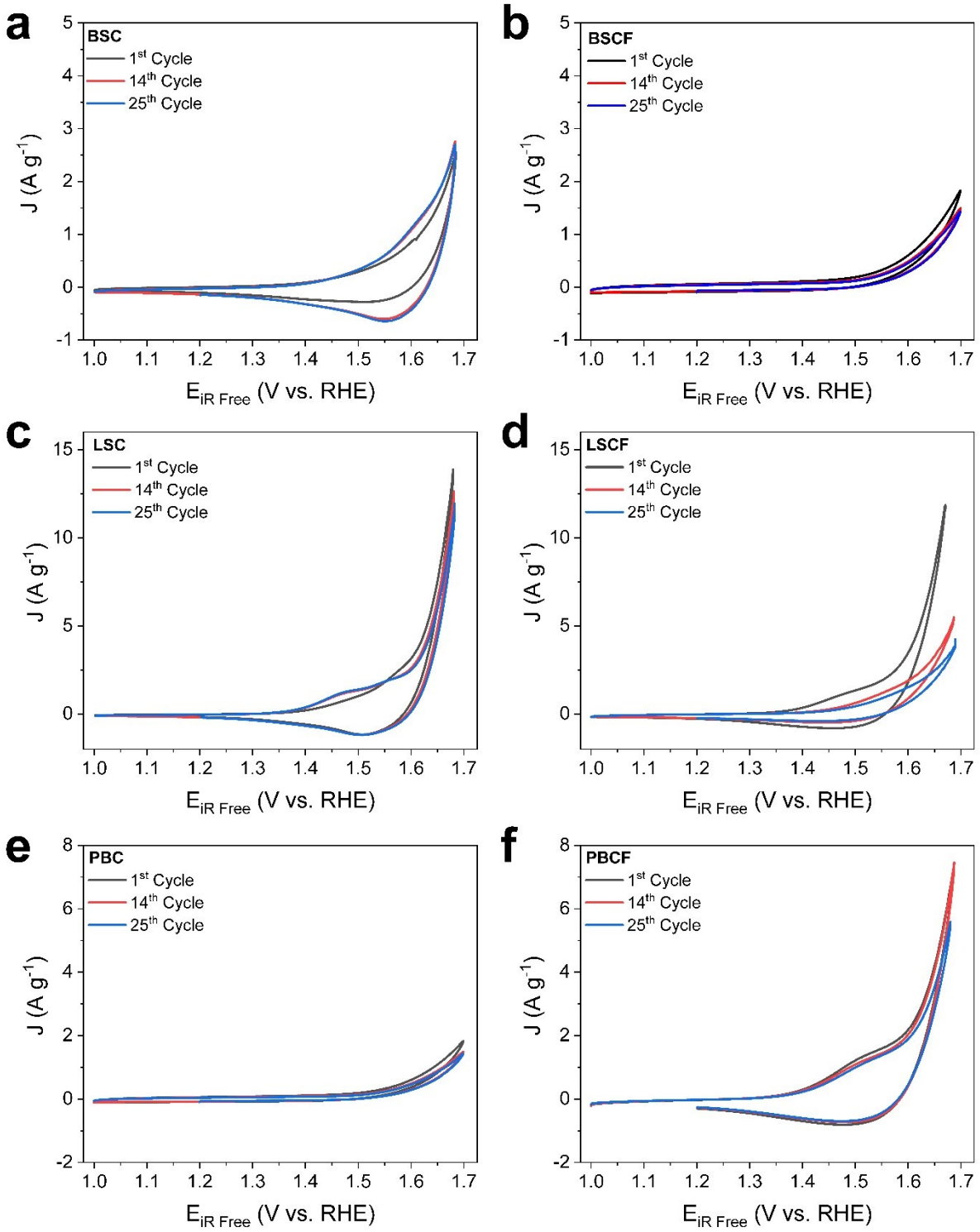


**Figure S2.** The initial cyclic voltammetry scanned at 10 mV $sec^{-1}$ from 1.0 to 1.7 $V_{RHE}$ at pH 7; a) BSC, b) BSCF, c) LSC, d) LSCF, e) PBC, and f) PBCF.

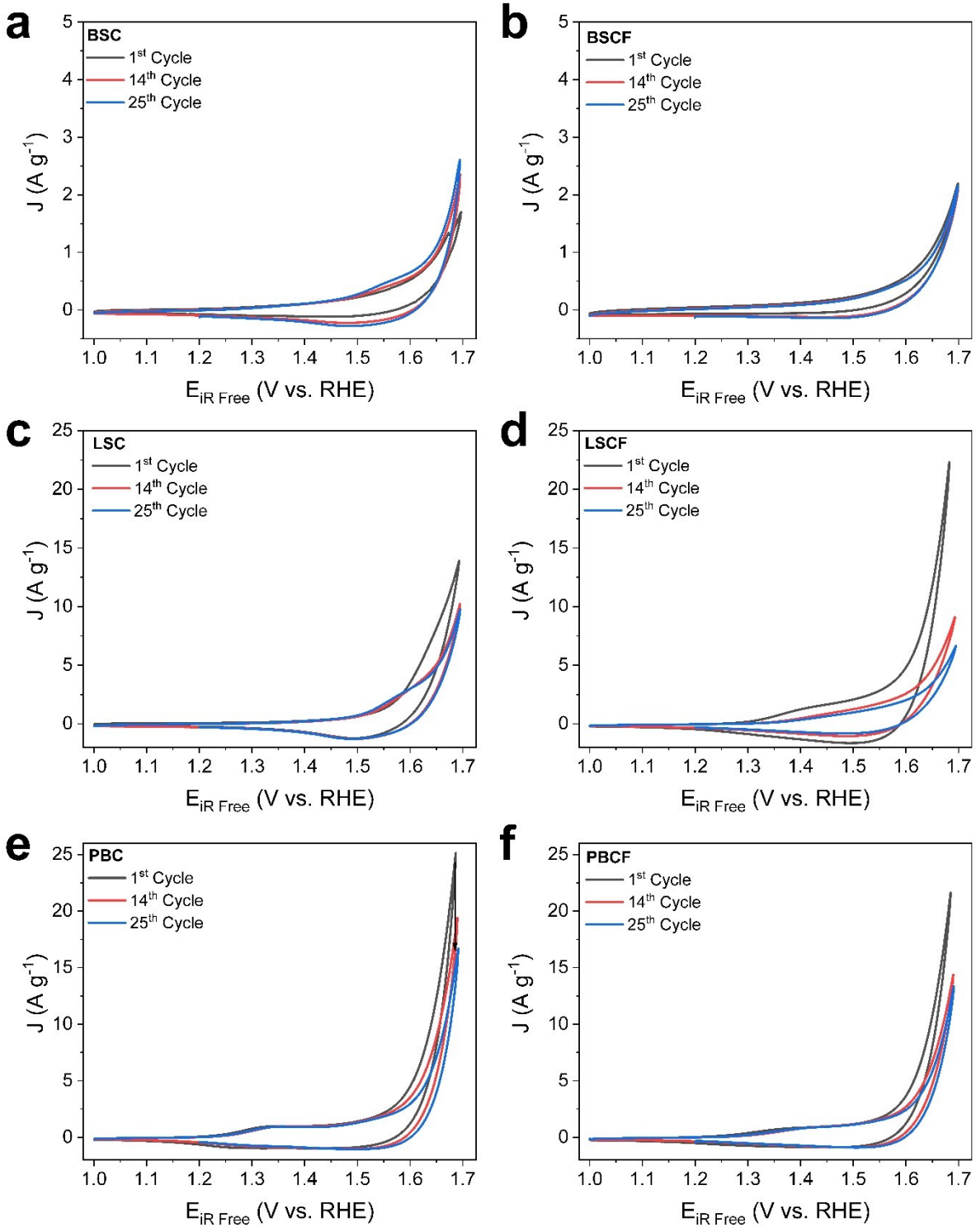


**Figure S3.** The initial cyclic voltammetry scanned at 10 mV $sec^{-1}$ from 1.0 to 1.7 $V_{RHE}$ at pH 9; a) BSC, b) BSCF, c) LSC, d) LSCF, e) PBC, and f) PBCF.

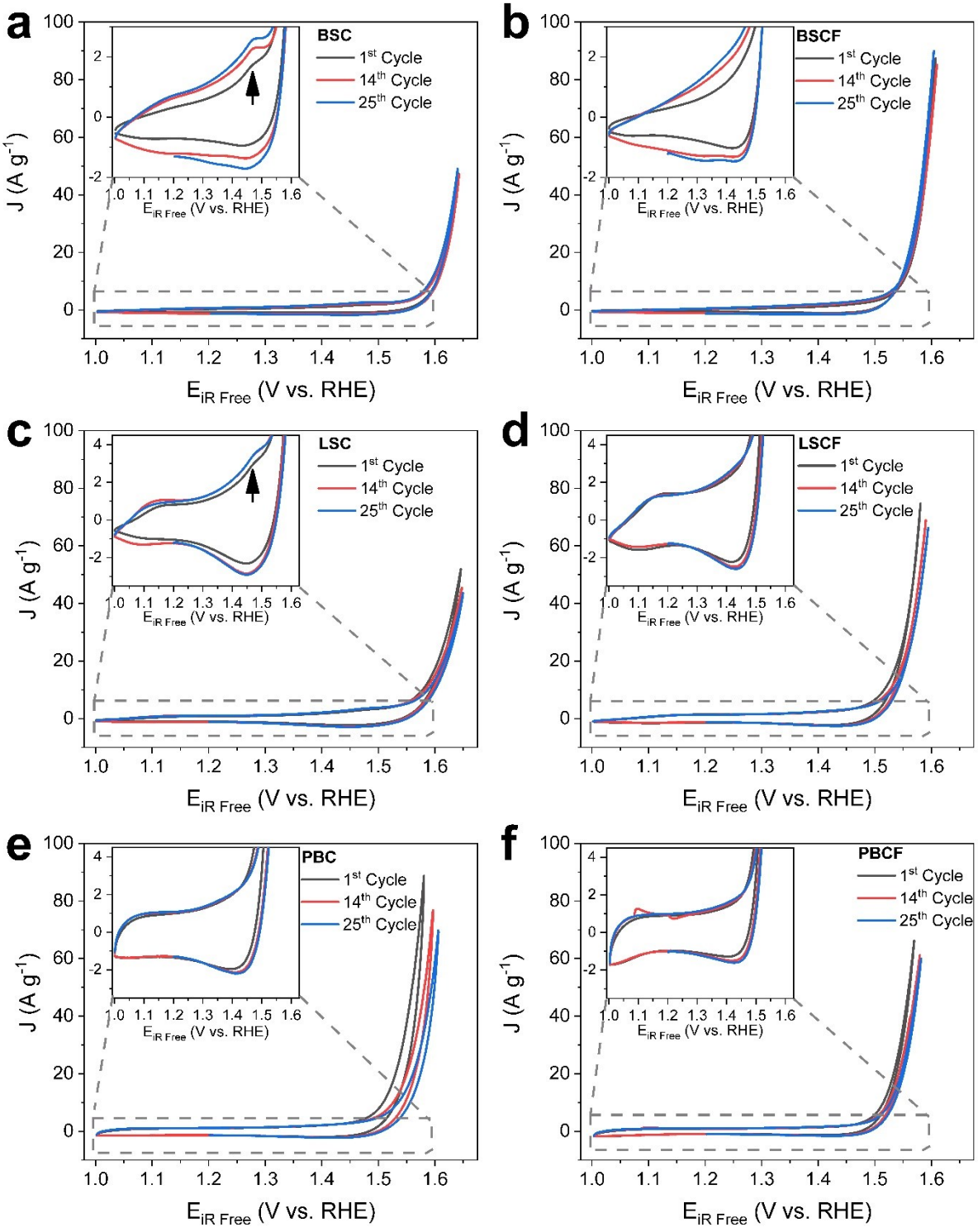


**Figure S4.** The initial cyclic voltammetry scanned at 10 mV $sec^{-1}$ from 1.0 to 1.7 $V_{RHE}$ at pH 13; a) BSC, b) BSCF, c) LSC, d) LSCF, e) PBC, and f) PBCF.

**4. Potential Stability Test**

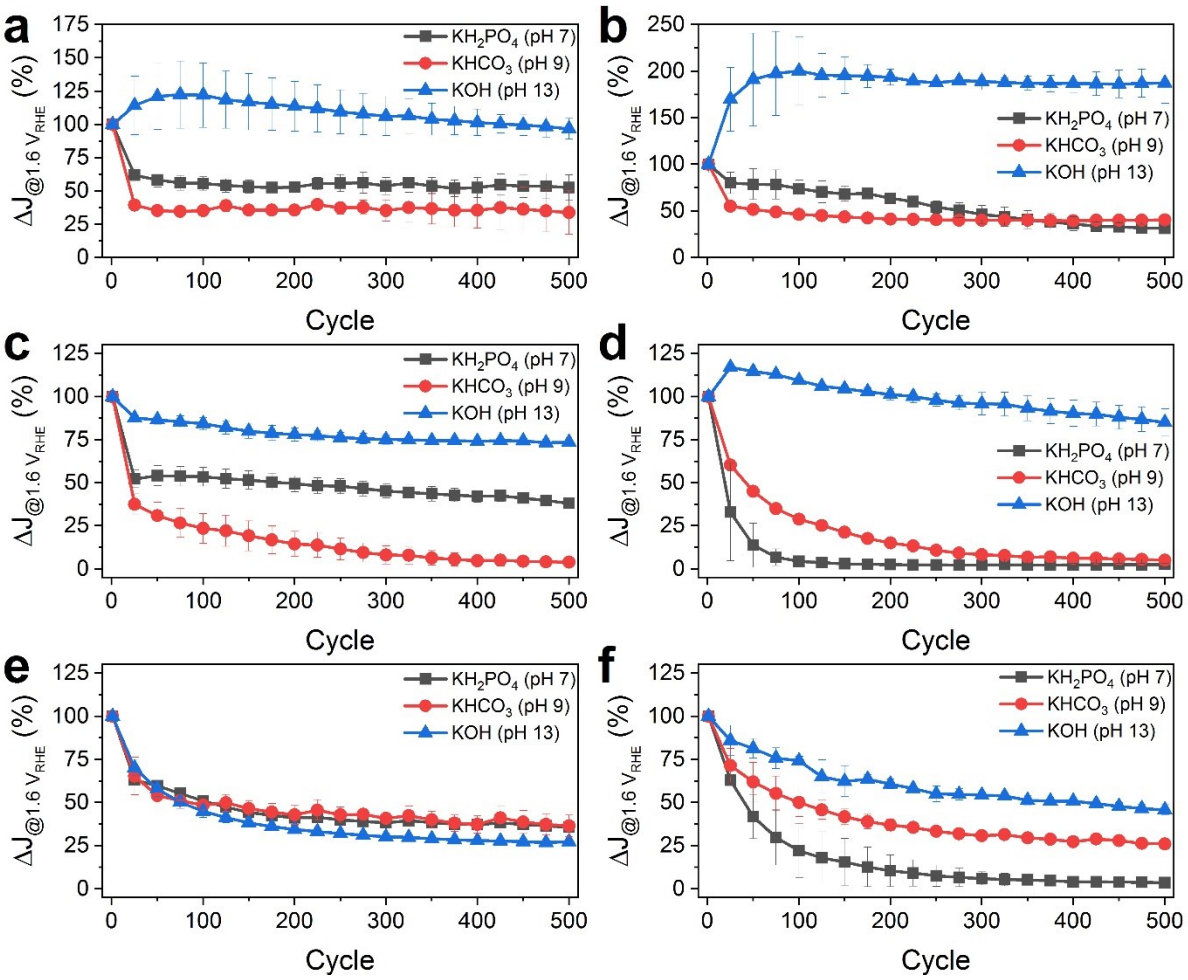


**Figure S5.** Mass normalized current densities recorded over 500 cycles at 1.6 $V_{RHE}$; a) BSC, b) BSCF, c) LSC, d) LSCF, e) PBC, and f) PBCF. Black, red, and blue lines shows the measurement at pH 7, 9, and 13, respectively. Figure 3 in the main manuscript represents the final changes in current density at the end of 500 cycles.

**5. Pourbaix Diagram – Density Functional Theory**

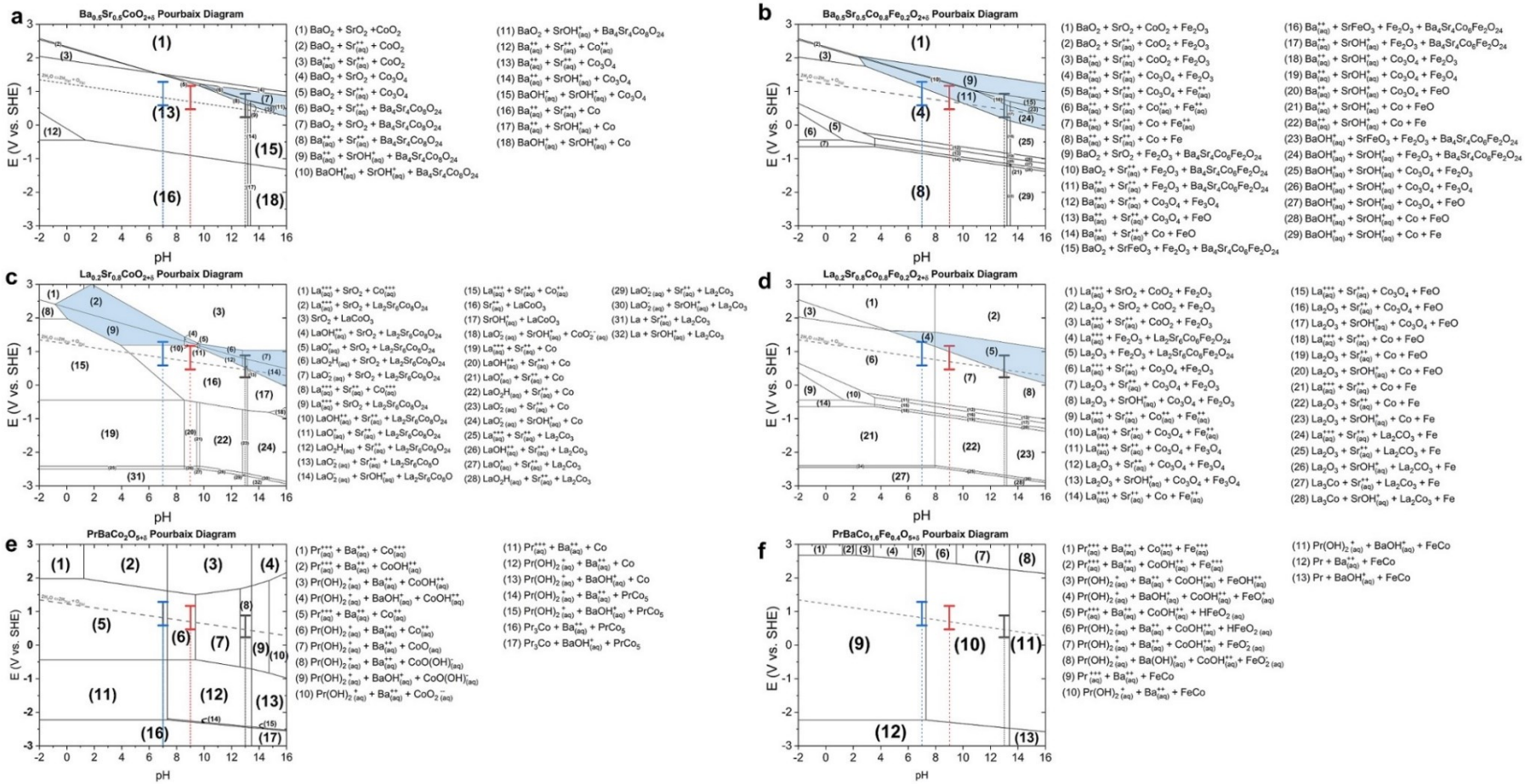


**Figure S6.** Density functional theory (DFT) calculated Pourbaix diagrams of a) $La_{0.2}Sr_{0.8}CoO_{3-\delta}$, b) $La_{0.2}Sr_{0.8}Co_{0.8}Fe_{0.2}O_{3-\delta}$, c) $Ba_{0.2}Sr_{0.8}CoO_{3-\delta}$, d) $Ba_{0.2}Sr_{0.8}Co_{0.8}Fe_{0.2}O_{3-\delta}$, e) $PrBaCoO_{6-\delta}$, and f) $PrBaCo_{2(1-x)}Fe_{2x}O_{6-\delta}$ (i.e. PBCF82 and PBCF55). Blue, red and black lines mark the ranges of the working potential (on standard hydrogen electrode (SHE) potential scale) for the oxygen evolution reaction (OER) at pH 7, 9, and 13, respectively. Shaded area in blue remarks the meta-stable phases of perovskite oxide. More details can be found in references [3, 4]

At pH 13, only $Ba_{0.5}Sr_{0.5}Co_{0.8}Fe_{0.2}O_{3-\delta}$ (BSCF) reveals that its oxygen evolution reaction potential lies within the thermodynamically meta-stable region (highlighted in blue) which explain the increasing current density during the stability cycle at pH 13. Related to its OER activity, the retained perovskite structure enables prolonged interfacial reaction during which Co-oxy(hydroxide) species are dynamically formed at the surface. On the contrary, the OER potential is not included in the meta-stability region for any other studied perovskites, which their thermodynamic instabilities under the OER conditions are anticipated. This disqualifies them as functionally stable catalyst considering prolonged operations. Even for BSCF, the OER potential is in its meta-stable region only at pH above 12.6. Given such small windows of thermodynamic meta-stability for these perovskites, the uniqueness of BSCF as promising OER catalyst is highlighted. [3, 5]

**6. Operando X-ray Absorption Near Edge Structure Spectra**

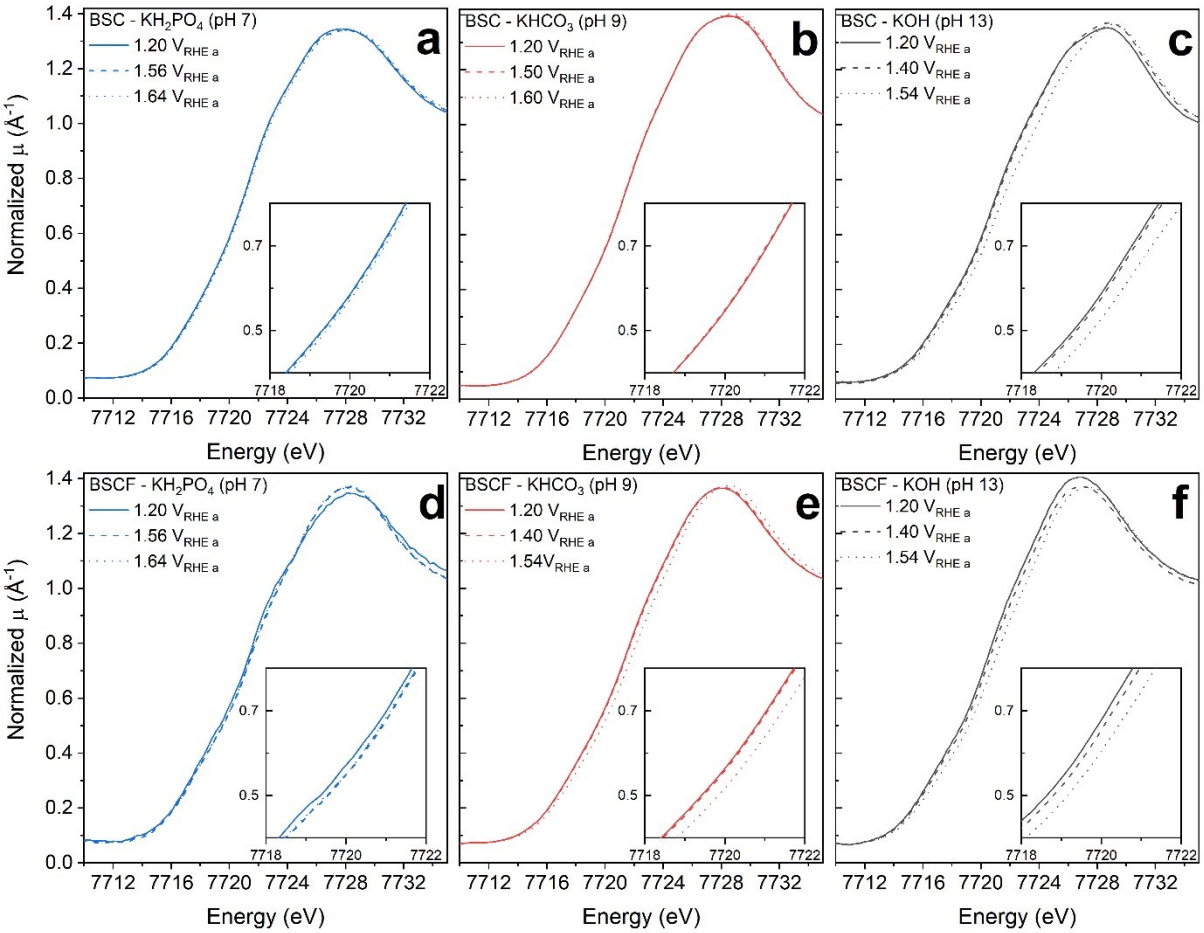


**Figure S7.** Comparisons of normalized X-ray absorption near edge structure (XANES) spectra at Co K-edge recorded at the initial 1.20 $V_{RHE}$, maximum anodic potential, and 1.20 $V_{RHE}$ after the subsequent cathodic polarization at pH 7, 9, and 13 for BSC (a – c, respectively) and BSCF (d – f, respectively). Each inset displays an enlarged view of the Co K-edge.

**7. Operando Extended X-ray Absorption Fine Structure Spectra Fittings**

FT-EXAFS spectra of BSC, and BSCF obtained during the operando flow cell tests were fitted using the Demeter software. Considering the EXAFS spectra equation below[6]

$$\chi(k) \propto \psi_{back.sc.}(0) = \sum_j \frac{S_0^2 * N_j * f_j(k) * e^{\frac{-2R_j}{\lambda(k)}} * e^{-2k^2\sigma_j^2}}{kR_j^2} sin\left[2kR_j + \delta_j(k)\right]$$

**Equation S1**

where $f_j(k)$, $\delta_j(k)$ and $\lambda(k)$ are scattering amplitude, phase shift, and mean-free path of photoelectrons, respectively, which depend on the absorber and backscatter atom and could be obtained from the theoretical model of a scattering pair. $N_j$, $R_j$, and $\sigma_j$ are structural parameters which would represent number of atoms in a shell j, radial distance from shell j, and mean square disorder of shell j at R, respectively. Finally, $S_0^2$ is amplitude reduction factor which is a non-structural parameter.

$S_0^2$ values were obtained from fitting the FT-EXAFS spectra of a reference metal (i.e. Co(0)) that is collected simultaneously with the FT-EXAFS spectra of each catalyst during the operando XAS study. The theoretical model were generated from Co-metal[7] to fit the reference metal, from which the $S_0^2$ were obtained for each reference FT-EXAFS spectrum. Then the $S_0^2$ value was used for fitting the rest of FT-EXAFS spectra of each respective perovskite catalyst. The FT-EXAFS profiles collected at 1.20 $V_{RHE}$ and at the maximum anodic potential are fitted to read any related changes. All of FT-EXAFS spectra were fitted in the range of 1- 3.3 Å, which the best fits are displayed in Figure S8 and S9 for BSC and BSCF, respectively. Table S2 summarizes the best fit parameters.

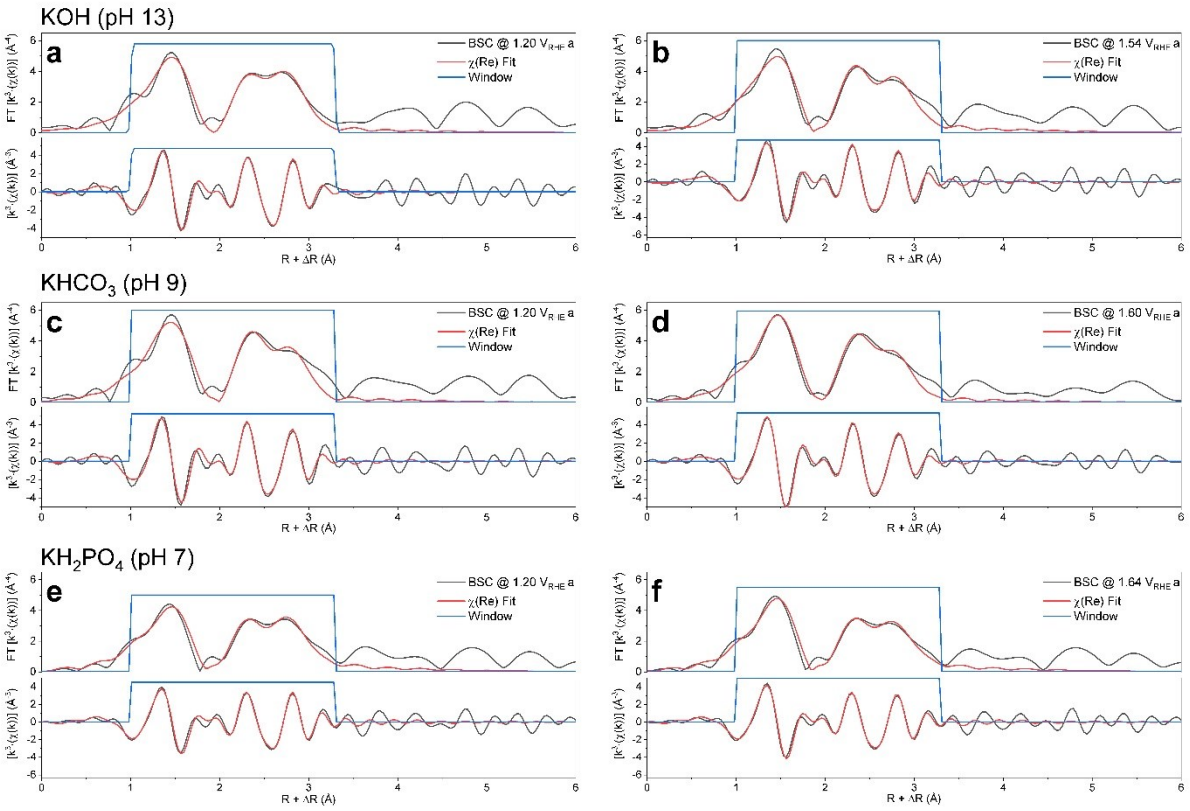


**Figure S8.** Fourier transformed $k^3$-weighted Co K-edge EXAFS spectra of BSC a – b) recorded at 1.2 and 1.54 $V_{RHE}$ anodic at pH 13, respectively; c – d) recorded at 1.2 and at 1.60 $V_{RHE}$ anodic at pH 9, respectively; and e – f) recorded at 1.20 and 1.64 $V_{RHE}$ anodic at pH 7, respectively. Black line is the FT-EXAFS spectrum, red line is the fitted spectrum, and blue is the window of the fitting.

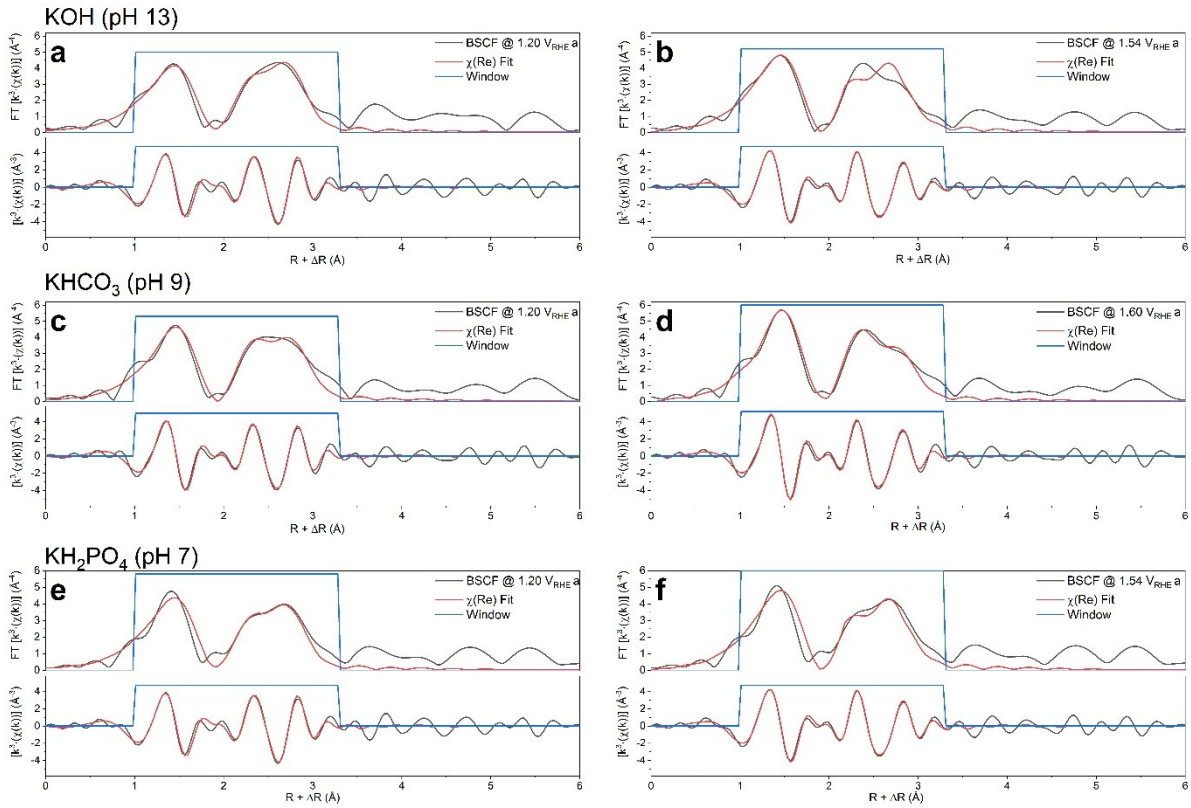


**Figure S9.** Fourier transformed $k^3$-weighted Co K-edge EXAFS spectra of BSCF a – b) recorded at 1.2 and 1.54 $V_{RHE}$ anodic at pH 13, respectively; c – d) recorded at 1.2 and at 1.60 $V_{RHE}$ anodic at pH 9, respectively; and e – f) recorded at 1.20 and 1.64 $V_{RHE}$ anodic at pH 7, respectively. Black line is the FT-EXAFS spectrum, red line is the fitted spectrum, and blue is the window of the fitting.

**Table S 2.** Summary of best fit parameters of the Fourier-transformed $k^3$-weighted Co K-edge EXAFS spectra recorded at 1.20 $V_{RHE}$ anodic and at the maximum anodic potentials at pH 13, 9, 7 for BSC and BSCF.

| Perovskite Catalysts | | Potentials | Co-O | | | Co-Co (CoOOH) | | | | Co-Co (Edge-sharing) | | | | R* |
|---|---|---|---|---|---|---|---|---|---|---|---|---|---|---|
| | | | $N_{Co-O}$ | R(Å) | $\sigma^2(Å)^2$ | $N_{Co-Co}{}^1$ | R(Å) | $\sigma^2(Å)^2$ | $\Delta E_0$ | $N_{Co-Co}{}^2$ | R(Å) | $\sigma^2(Å)^2$ | $\Delta E_0$ | |
| BSC | pH 13 | **1200 mV A** | 5.4(0.4) | 1.91(0.015) | 0.008(0.004) | 3.0(0.5) | 2.84(0.011) | 0.006(0.003) | -6(2) | 3.0(0.5) | 3.04(0.001) | 0.005(0.003) | 2(3) | 0.020 |
| | | **1540 mV A** | 6.2(0.5) | 1.91(0.010) | 0.008(0.002) | 2.6(0.4) | 2.83(0.019) | 0.004(0.003) | -5(2) | 2.6(0.4) | 3.04(0.001) | 0.003(0.003) | 4(4) | 0.020 |
| | pH 9 | **1200 mV A** | 5.5 (0.4) | 1.91(0.008) | 0.007(0.003) | 2.9(0.5) | 2.83(0.017) | 0.006(0.006) | -4(2) | 2.9(0.5) | 3.05(0.010) | 0.005(0.005) | 6(4) | 0.026 |
| | | **1600 mV A** | 5.5(0.4) | 1.91(0.008) | 0.007(0.003) | 2.9(0.6) | 2.84(0.012) | 0.005(0.005) | -5(2) | 2.9(0.5) | 3.04(0.007) | 0.005(0.003) | 6(4) | 0.026 |
| | pH 7 | **1200 mV A** | 5.6(0.4) | 1.91(0.016) | 0.011(0.004) | 2.1(0.4) | 2.83(0.020) | 0.003(0.003) | -6(2) | 2.1(0.3) | 3.03(0.012) | 0.002(0.003) | 2(4) | 0.015 |
| | | **1640 mV A** | 5.3(0.3) | 1.91(0.010) | 0.009(0.003) | 1.9(0.3) | 2.85(0.023) | 0.003(0.002) | -4(2) | 1.9(0.3) | 3.04(0.012) | 0.002(0.001) | 4(3) | 0.010 |
| BSCF | pH 13 | **1200 mV A** | 5.1(0.5) | 1.91(0.015) | 0.011(0.004) | 2.4(0.6) | 2.84(0.012) | 0.006(0.003) | -6(3) | 3.7(0.8) | 3.03(0.014) | 0.006(0.004) | -1(4) | 0.021 |
| | | **1540 mV A** | 5.5(0.3) | 1.91(0.011) | 0.010(0.011) | 2.8(0.4) | 2.84(0.010) | 0.010(0.010) | -4(2) | 3.0(0.4) | 3.03(0.010) | 0.005(0.002) | 0(3) | 0.006 |
| | pH 9 | **1200 mV A** | 4.6 (0.3) | 1.91(0.015) | 0.008(0.003) | 2.7(0.4) | 2.85(0.023) | 0.006(0.003) | -5(2) | 2.7(0.4) | 3.04(0.007) | 0.005(0.003) | 2(4) | 0.015 |
| | | **1600 mV A** | 4.5(0.5) | 1.91(0.009) | 0.007(0.003) | 2.9(0.4) | 2.85(0.004) | 0.006(0.003) | -4(2) | 2.9(0.5) | 3.04(0.003) | 0.006(0.003) | 2(3) | 0.011 |
| | pH 7 | **1200 mV A** | 4.7(0.4) | 1.92(0.028) | 0.006(0.004) | 3.6(0.8) | 2.85(0.025) | 0.008(0.007) | -3(2) | 3.4(0.8) | 3.04(0.009) | 0.007(0.007) | 5(5) | 0.027 |
| | | **1540 mV A** | 4.9(0.5) | 1.92(0.025) | 0.007(0.002) | 3.5(0.6) | 2.84(0.003) | 0.006(0.003) | -3(2) | 3.5(0.5) | 3.04(0.006) | 0.006(0.003) | 5(4) | 0.020 |

* Note that R-factor is a statistical value used to quantitatively evaluate the quality of fits. The numbers in brackets represent ± error obtained provided by the Artemis program of the Demeter software.[3]

On the other hand, it was mentioned in the main manuscript that other perovskites (i.e. LSC, LSCF, PBC, and PBCF), were not included in this study due to the coinciding Co–Co bond distance between the edge-sharing polyhedra in perovskite structure and that of Co-O(OH) (~2.8 Å). To explain this better Figure S10 is created. To elaborate, in the presence of oxygen non-stoichiometry within perovskite structure for having a high concentration oxygen vacancy, the B-site metal octahedra would be reorganized to a more stable network by rearranging neighboring polyhedra to share its oxygen edges.[8] Consequently, the distance between Co–Co is shortened where the Co–Co distance in the edge-sharing polyhedra is ($a' = a/\sqrt{2}$ as calculated by a simple trigonometry and summarized in Table S2. Coincidentally, the estimated Co–Co distances of the edge-sharing polyhedra of these layered double perovskites are close to that of Co-oxy(hydroxide) (~2.8 Å).[9-11] Consequently, this coinciding Co–Co distances between the edge-sharing polyhedra and Co-oxy(hydroxide) limits our interpretation of the changes observed in FT-EXAFS spectra under the operando conditions (see Figure S8).

**Table S3.** Lattice parameters of LSC, LSCF, PBC, and PBCF calculated from Rietveld refinement of their X-ray diffractions. With the estimated lattice parameter, the Co–Co distance of edge-sharing polyhedron is calculated.

| Perovskite Oxide | *a*<br>Co-Co/Fe<br>corner-shared<br>octahedron (Å) | *a'*<br>Calculated Co-Co/Fe<br>edge-shared polyhedron (Å) |
|---|---|---|
| LSC | 3.8272 | 2.706 |
| LSCF | 3.8417 | 2.717 |
| PBC | 3.8766 | 2.741 |
| PBCF | 3.8891 | 2.750 |

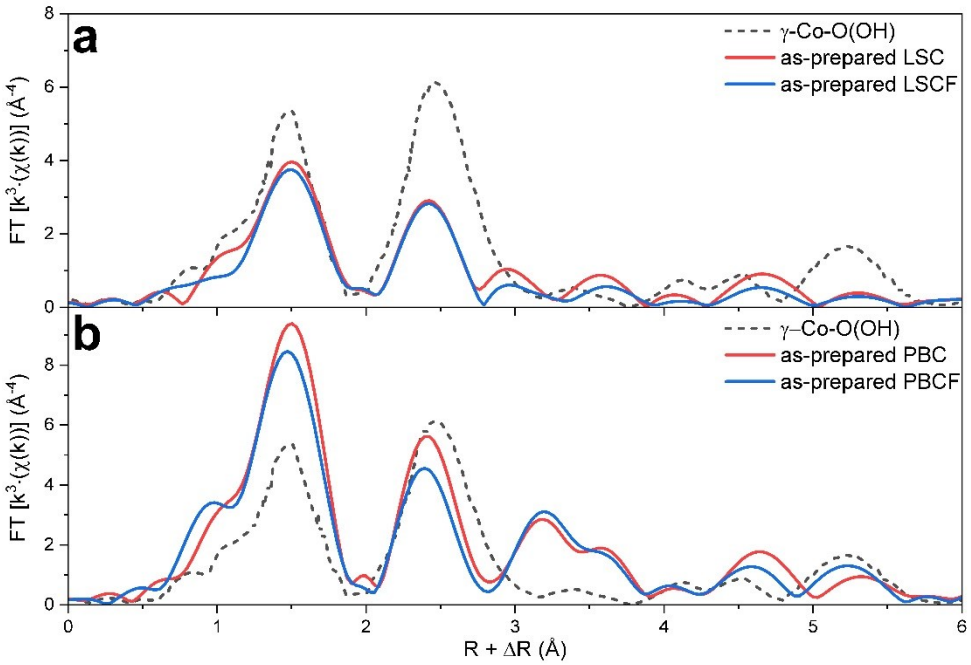


**Figure S10.** Comparison of Fourier transformed (FT) $k^3$-weighted EXAFS profiles at Co K-edge of γ-Co-O(OH)[9] with as-prepared perovskite catalysts a) LSC and LSCF; b) PBC and PBCF.

**References**


1. A. C. Tomkiewicz, M. A. Tamimi, A. Huq and S. McIntosh, *Solid State Ionics*, 2013, **253**, 27-31.
2. Y. Wang, L. Yu, J. H. Wang, L. W. Chen, W. G. Gao, X. L. Du and L. H. Biao, *Mater. Lett.*, 2012, **75**, 39-41.
3. B.-J. Kim, E. Fabbri, D. F. Abbott, X. Cheng, A. H. Clark, M. Nachtegaal, M. Borlaf, I. E. Castelli, T. Graule and T. J. Schmidt, *Journal of the American Chemical Society*, 2019, **141**, 5231-5240.
4. B. J. Kim, X. Cheng, D. F. Abbott, E. Fabbri, F. Bozza, T. Graule, I. E. Castelli, L. Wiles, N. Danilovic, K. E. Ayers, N. Marzari and T. J. Schmidt, *Adv. Funct. Mater.*, 2018, **28**.
5. E. Fabbri, M. Nachtegaal, T. Binninger, X. Cheng, B. J. Kim, J. Durst, F. Bozza, T. Graule, R. Schaublin, L. Wiles, M. Pertoso, N. Danilovic, K. E. Ayers and T. J. Schmidt, *Nat. Mater.*, 2017, **16**, 925.
6. J. J. Rehr and R. C. Albers, *Rev. Mod. Phys.*, 2000, **72**, 621-654.
7. G. I. Kulesko and A. L. Seryugin, *Phys. Metals. Metallog.*, 1968, **26**, 140.
8. T. C. Gibb, *J. Mater. Chem.*, 1992, **2**, 387-393.
9. J. H. Huang, Q. H. Liu, T. Yao, Z. Y. Pan and S. Q. Wei, *J. Phys. Conf. Ser.*, 2016, **712**, 012128.
10. J. H. Huang, Q. C. Shang, Y. Y. Huang, F. M. Tang, Q. Zhang, Q. H. Liu, S. Jiang, F. C. Hu, W. Liu, Y. Luo, T. Yao, Y. Jiang, Z. Y. Pan, Z. H. Sun and S. Q. Wei, *Angew. Chem. Int. Edit.*, 2016, **55**, 2137-2141.
11. D. Totir, Y. B. Mo, S. Kim, M. R. Antonio and D. A. Scherson, *J. Electrochem. Soc.*, 2000, **147**, 4594-4597.